

Investigation of Modeling Approaches to High-Fidelity Computational Predictions of Tiltrotor / Obstacle Aerodynamic Interactions

Alex M. Moushegian
Aerospace Engineer

David M. Farish
Aerospace Engineer
Naval Air Warfare Center Aircraft Division
Patuxent River, MD, USA

Eric W. Hayden
Rotary Wing Team Lead

Andrew L. Bodling
Research Scientist
Science and Technology Corporation
Moffett Field, CA, USA

ABSTRACT

A new framework for performing high-fidelity computational aeromechanics simulations of the V-22 tiltrotor aircraft in vertical take-off and landing mode has been developed. It is built on the HPCMP CREATE-AV Helios tool and utilizes scripted input generation and automatic replacement of modular model components. This new framework has been used to investigate the impact of various approaches to modeling the rotor and obstacle aerodynamics on predictions of aircraft performance in hover near a large ground obstacle. This work builds upon the results of a previous study of modeling fidelity requirements for predicting hover performance in ground effect. The findings indicate that a medium-fidelity simulation utilizing actuator line blades and an immersed boundary obstacle can provide rotor performance predictions and flow field features with comparable accuracy to a fully-meshed approach. Analysis of the physical phenomena in these recirculating flows and a brief analysis into the mechanisms for rotor performance loss are also provided. The computational framework accurately captures trends in rotor loads and airframe download from flight test data within approximately 5%. The medium-fidelity approach required 83% fewer computational resources, representing a 6X speedup.

INTRODUCTION

The shipboard environment in which naval rotorcraft operate, often referred to as the dynamic interface (DI), is characterized by complex and unsteady flow fields generated as a result of the coupling between rotor wakes and the ship airwake. Just as the turbulence and recirculation in the ship airwake modifies the inflow of the rotor(s), the rotor outwash impinging on the sea surface, hull, flight deck, and/or hangar face in turn modifies the ship airwake. These coupled interactions can impact aircraft performance and handling qualities in unexpected and detrimental ways. The impacts of the DI on rotorcraft include increased pilot workload and limitations on launch-and-recovery envelopes (LREs) (Ref. 1). Modeling and simulation (M&S) tools like Computational Fluid Dynamics (CFD) offer naval engineers the ability to model these complex flow environments and potentially reduce technical, cost, and schedule risks associated with shipboard flight testing (Ref. 2).

The present work was performed in conjunction with the efforts of the Office of Naval Research (ONR)-funded Dynamic

Interface Virtual Environment (DIVE) program to develop, validate, and implement DI M&S tools to support DI flight testing. The ultimate goal of the DIVE program was to reduce the resources required to generate LREs (Ref. 3). LREs define the wind-over-deck (WOD) conditions in which aircraft can safely take off and land aboard air-capable ships. To effectively apply CFD to the generation of LREs, the modeling techniques must first be quantitatively assessed against full-scale DI testing with naval rotorcraft. As the transition platform for the DIVE program, the Bell-Boeing MV-22B Osprey is the focus of the present work. Previous work has been completed to develop and validate a computational model of V-22 aeromechanics that can accurately predict aircraft interactions during in-ground-effect (IGE) hover (Ref. 4). The present work is part of a new computational study that builds upon those findings and other DIVE efforts and applies the model to more severe wake-obstacle interactions where rotor downwash recirculation is present.

During shipboard operations, as rotorcraft hover over landing spots or cross deck edges, the downwash impinges on the surface below the aircraft and climbs the vertical surfaces of the ship structures. In some instances, instead of convecting away, the rotor downwash rises above the vehicle and is reingested into the rotor system. The DIVE program has funded multiple small-scale tests to study the effects of this phenomenon,

Presented at the Vertical Flight Society's 81st Annual Forum & Technology Display, Virginia Beach, Virginia, May 20–22, 2025. This is a work of the U.S. Government and is not subject to copyright protection in the U.S.

namely the Coupled Rotor/Upwind Ship Aerodynamic Interaction Data (CRUSAID) (Ref. 5) test and the Bihrl Applied Research Low-Speed Obstacle-Induced Downwash Recirculation (BAR LOIDR) 6% test (Ref. 6). These subscale data were used for CFD model validation for recirculating flows in previous work (Ref. 7). In this previous study, it was found that actuator line rotor blade modeling is sufficient for capturing aircraft performance with the same accuracy as meshed-blades, and that modeling the obstacle as an immersed boundary with simple stair-step boundary conditions can introduce significant deficiencies in the modeled physics when the aircraft is close to the obstacle. Therefore, a fully-meshed obstacle or more advanced immersed boundary conditions are required to accurately capture tiltrotor aircraft performance in recirculating flows. Regardless of the modeling fidelity, the simulations failed to capture a torque benefit in deep ground effect near the obstacle that was observed in the test data, and no clear cause was identified.

Small scale testing offers greater control over experimental parameters and thus the phenomena of interest. However, such testing may have limitations on key scaling parameters (e.g. Reynolds and Mach numbers). To further understand the physics of rotor downwash recirculation, full-scale investigations are required. This work will describe modeling fidelity studies at full scale similar to those performed with the subscale test data to determine whether the same conclusions hold, or if model size has an impact on modeling fidelity requirements.

VALIDATION DATASET

In the fall of 2020, the Navy conducted a flight test at Naval Air Station (NAS) Patuxent River to investigate rotor/obstacle interactions in low-wind conditions, pictured in Fig. 1 (Ref. 8). While several type/model/series rotorcraft were analyzed in this test, this work focuses on the V-22. The test utilized the loads-instrumented aircraft, which provided useful data channels in addition to those included onboard the standard fleet aircraft. In particular, the loads aircraft has rotor yoke beam bending gauges that provide a derived measurement of individual rotor thrust. The aircraft flight data were recorded via an onboard Airborne Data Acquisition System (ADAS), and aircraft position and orientation were provided by the Advanced Range Data System (ARDS).

To acquire a baseline of the V-22's performance, the test pilots flew isolated hover ladders at the beginning and end of each test day. These isolated hover ladder cases provided excellent validation data for establishing computational modeling tradeoffs and best practices for the rotors and airframe, as described in Ref. 4. The obstacle in the test was an Elevated Fixed Platform (EFP), built out of CONEX shipping containers. The dimensions of the EFP were 99.4ft wide, 95.4ft deep, and 38.0ft tall. When an aircraft was operating above the EFP, the aerodynamic interactions were intended to represent operations near an LPD 17 flight deck edge. The aircraft could also be flown alongside the EFP, representing operations over



Figure 1: Full-scale wake-obstacle interaction flight test at NAS Patuxent River, via Ref. 8

deck near closed hangar doors on the LPD 17. The latter test points were the focus of this study.

The primary performance metrics extracted from the flight test data were rotor thrust and torque and airframe download. Since airframe download was not directly measured, it was derived by subtracting the vertical components of rotor and empirically-derived engine exhaust jet thrust from the aircraft gross weight. Despite uncertainty in both the measured rotor thrust and the derived engine exhaust jet thrust, the derived download per unit thrust agreed with previous experimental measurements out of ground effect (OGE) (Ref. 9).

TRANSLATING FLIGHT TEST DATA TO CFD INPUTS

The flight test program recorded data for many hover positions at three gross-weight (GW) bands (see Table 1). This study focuses on the heavy-gross-weight band. The majority of testing was conducted with light-and-variable winds, using a knock-it-off wind limit of 5 knots. The following sections describe the methods used to convert the time-varying flight test data into meaningful parameters that could be input into the CFD simulations.

Test Record Data Reduction

The flight test data presented in this study came from the V-22's onboard data acquisition systems. A more detailed description of these systems is provided in (Ref. 8). The important parameters to match in the simulations are the aircraft nacelle angle, position, orientation, blade pitching/flapping, and rotor thrust/torque. Details of the data reduction technique for this test are described in Ref. 4.

CFD Case Generation

The flight test data were averaged over each test record and reduced to a limited set of parameters that were used as inputs to an automated CFD case-generation procedure. These parameters were fuselage position, fuselage attitude, left and right rotor cyclic pitching and flapping, and left and right rotor thrust. The inputs for simulations at each hover position were

Table 1: Table of gross weight band definitions for flight test.

GW Band	Power Margin	Mast Torque
Heavy	25%	92.4%
Mid	37%	80.4%
Light	48%	69.4%

generated from these parameter values automatically by modifying a set of template inputs via the Helios case generation framework described in Ref. 4.

COMPUTATIONAL APPROACH

The complexity of the tiltrotor system necessitated a flexible computational framework with extensive capabilities. The High Performance Computing Modernization Program (HPCMP) provides a suite of computational tools called the Computational Research and Engineering Acquisition Tools and Environments (CREATE). Among these tools is Helios, a program dedicated to computational analysis of rotorcraft aeromechanics. Helios is a python interface between a set of component libraries that handle various tasks within a rotorcraft aeromechanics simulation, including fluid solvers, structural solvers, domain connectivity routines, mesh motion handling, co-processed outputs, and more (Ref. 10). The compartmentalized nature of Helios makes modeling the complicated tiltrotor system manageable as a user, as the components can be developed independently and added to the total model as needed. Helios version 12.2.1 was utilized in this work.

The Helios framework was leveraged to easily modify the aircraft position and orientation relative to the EFP, apply rotor control inputs and thrust targets measured from the flight test data, and vary rotor and obstacle modeling techniques to investigate the modeling fidelity required to capture the performance impact of rotor downwash recirculation. The computational approach for the V-22 used in this effort was largely based on the results of the authors' previous work (Ref. 4).

Airframe Modeling Approach

To resolve the airframe near-body fluid dynamics, a “body-fitted” method, utilizing the unstructured, unsteady Reynolds-Averaged Navier-Stokes (uRANS) solver kCFD (Ref. 11), computed the aerodynamic interactions of the rotor wake and ground/obstacle effects with the airframe. A body-fitted mesh with kCFD captures the download on the airframe with significantly more accuracy than an immersed-boundary method (IBM) with a stair-step implementation (Ref. 4). For this reason, IBM was not used to model the airframe in the present study. The V-22's nacelle angle was set to the average nacelle position recorded during every flight test point. Because each flight test point had approximately the same average nacelle angle of 88°, only a single V-22 mesh was required. The flight test data also informed the aircraft attitude and placement in the simulations; for each test record, time averaged ARDS values prescribe the airframe position and orientation with respect to the EFP.

EFP Modeling Approach

The EFP near-body fluid dynamics were resolved via two methods. The first method used the same “body-fitted” method as that employed for the airframe. A preliminary study of the fidelity required in the body-fitted EFP model showed that the small-scale aerodynamic features (e.g. corrugation of the shipping containers) had little to no impact on the gross aerodynamic flow-field induced by a rotorcraft operating near the structure. The computational cost associated with modeling small features of the stacked shipping containers was not justified given the similarity in flow field predictions, and therefore the EFP was represented by a smooth rectangular prism of the appropriate dimensions. The second method modeled the EFP as an immersed boundary within the off-body mesh via the Reduced-Order Aerodynamic Model (ROAM) module in Helios (Ref. 10).

Unstructured uRANS solvers commonly utilized in body-fitted methods are limited to second-order spatial accuracy, and therefore require dense computational grids to compute accurate aerodynamics. Additionally, to compute accurate surface forces, any body-fitted method requires point clustering near solid walls to resolve the aerodynamic boundary layer. Immersed boundary methods typically do not aim to resolve the boundary layer, as was the case in this study, and may or may not use a wall model as an approximation. Therefore, they tend not to be reliable methods for computing surface forces. IBM can, however, provide gross blockage effects for upstream rotors and predict general trends in body aerodynamics. These compromises are acceptable for the current application as long as the IBM can accurately predict the behavior of the rotor wash as it impinges on the ground obstacle, which will be established by the results of the current study.

Rotor Blade Modeling Approach

The rotor blade near-body fluid dynamics were resolved via two different methods. The first method, called “meshed blades,” used the structured-curvilinear uRANS solver OVERFLOW (Ref. 12) to directly model the rotor blade aerodynamics by resolving the blade surface as it moves through the flow field. The second method, called “actuator line,” used another capability of ROAM to represent the rotor blades as momentum sources in the flow field whose strength is based on a blade-element representation of the rotor blades (Ref. 10). In the ROAM actuator line rotor model, the momentum sources are located along the instantaneous quarter-chord lines of the blades as they rotate around the rotor hub and are applied within an off-body flow solver, described in the next section. This is a medium-fidelity alternative to the lower-fidelity actuator disk method, where the rotor-induced momentum is applied across the entire rotor disk (Ref. 13). Collocating the momentum sources with the blade location allows actuator line methods to capture the tip vortices and helical structure of the rotor wake, and resolve unsteady blade aerodynamic response associated with blade

passage. These effects cannot be accurately resolved with actuator disks, though actuator disks have a less strict requirement on the computational time step and can be applied in a steady-state calculations. Meshed-blade methods, on the other hand, have an even stricter constraint on time step, limited by the changing interpolation stencils of the overlapping near-body and off-body grid systems that are in relative motion as well as by the motion of the cells on the blade surface that generate the wake.

Blade collective pitch was modeled with a “trimmed collective” method that used the Rotorcraft Comprehensive Analysis Solver (RCAS) to control the rotation of nodes in a simple rigid beam-element model of the aircraft based on a combination of prescribed blade motion and a collective pitch controller that trims to a target thrust on each rotor. The target thrust values for each rotor came from the time-averaged flight-test-derived data at each hover height. The lateral and longitudinal cyclic pitch and flapping motion was prescribed based on the time-averaged values recorded in the flight test.

Off-body Modeling Approach

The off-body fluid dynamics were resolved with SAMCart, which employs a fully-Cartesian overset mesh system (Ref. 14). The SAMCart domain contained a static refinement region encompassing a large volume around the aircraft and EFP. To ensure a mesh-independent solution, the vertical extent of this region was tested with values of 60 ft and 148 ft. Figure 2 shows the effect of the vertical extent of the off-body static refinement region with the V-22 operating with a blade tip clearance to the EFP of 1.3R and 4R, where R is the radius of the V-22 rotor. As shown in the figure, the 148-ft vertical extent resolves the full recirculatory trajectory of the rotor wash and was therefore chosen for this study.

The boundary condition applied to the ground surface was also varied between an inviscid and viscous boundary condition. Modeling the ground plane as an inviscid boundary resulted in a 1% difference in rotor thrust and a negligible difference in torque and figure of merit in the V-22 compared to simulations with a viscous ground plane. However, in cases using the viscous ground plane, slightly less outwash and recirculation were observed, and the tip vortex trajectory was more clearly defined. To model the ground as a viscous surface, simulations required 50% more CPU resources than equivalent simulations using an inviscid ground plane. Based on these observations, all subsequent simulations used an inviscid ground plane in the off-body domain.

Final Modeling Approach

Due to the large matrix of cases, model variation was performed by choosing either a fully-meshed high-fidelity paradigm (meshed-blades and body-fitted EFP) or a mid-fidelity paradigm (actuator line blades and immersed boundary EFP), as described in Table 2. In either case, engine exhaust jet thrust was not included in the computational models, as it is a second-order effect on aircraft performance and can

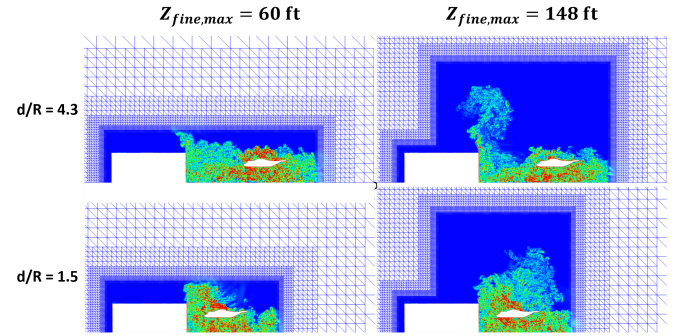


Figure 2: Effect of off-body mesh z-extent.

Table 2: Table of modeling approaches in the Mid- and High-Fidelity Simulations.

Fidelity	Rotors	Airframe	EFP
High	Meshed Blades	Body-Fitted	Body-Fitted
Mid	Actuator Line	Body-Fitted	IBM

be accounted for empirically when calculating the predicted aircraft performance.

Computational Meshes

The SAMCart off-body mesh was constructed at run-time based on the aircraft position relative to the EFP. The static refinement region contained 0.2-foot cells and corresponded to the bounding box with the following extrema:

- Longitudinal: EFP midpoint to 3 rotor radii (R) aft of the rotor hubs
- Lateral: minimum of 2R port of the rotor hubs and 1R port of the EFP port edge to 1R starboard of the EFP starboard edge.
- Vertical: ground to 7.8R above the ground.

Outside of the static refinement regions, the cell sizes grow geometrically to the far field boundaries 2,048 ft ($>100R$) from the area of operations in all directions, where a zero-wind characteristic far field boundary condition is applied. The off-body mesh size varied between 511 million and 886 million unique nodes (i.e. not including duplicate fringes from mesh parallel decomposition) depending on the aircraft hover position; an example is shown in Fig. 3. The off-body grid size when including duplicate fringes exceeded 1 billion nodes in many cases.

The airframe unstructured kCFD mesh was generated in AFLR3 (Ref. 15) with wing flaps at 72 degrees and nacelles at 88 degrees based on the measured states of these parameters during the flight test. The development of the mesh followed engineering best practices, with a first cell size meeting the $y^+ = 1$ condition in the wall-normal direction, and clustering of points near high aerodynamic and geometric gradients. To leverage Helios’s ability of integrating multiple specialized solvers, the V-22 mesh was trimmed to a wall distance

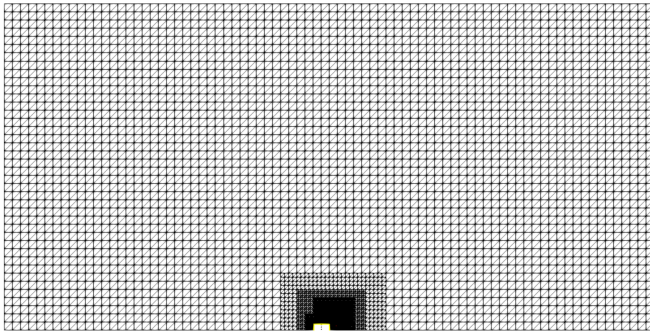


Figure 3: Slice of the off-body mesh demonstrating the domain extents and refinement relative to the EFP.

of approximately 2 ft. The airframe mesh had a total of 110.5 million cells, and can be observed in Fig. 4. Features on the airframe smaller than six inches were neglected with the assumption that they have a negligible impact on download and do not change the impact of recirculation on aircraft performance. A previous internal study used the same grid topology settings to generate a reduced order model for recovery of the V-22 to a US Navy ship with great success. The present study only modified the nacelle angle; no other mesh settings were changed. This includes the landing gear remaining stowed, though the flight test was performed with landing gear down. The impact of this configuration discrepancy was not quantified.

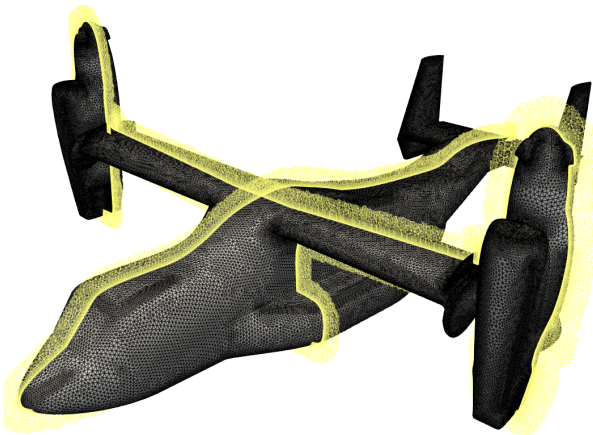


Figure 4: Unstructured mesh representation of the V-22 airframe.

The unstructured kCFD mesh for the EFP followed the meshing best practices used for ship airwake/bluff body analyses. The EFP maintained a first-cell wall-normal spacing of $y^+ = 1$ over the entire structure and a surface spacing of 1 ft with extra refinement added to the edges (0.25-ft spacing). The near-body volume sizing matched the finest region of the Cartesian off-body grid. Similar to the airframe near-body unstructured mesh, the EFP volume mesh was trimmed to a wall distance of approximately 2.5 ft to maximize utilization of the more efficient Cartesian off-body solver. Figure 5 shows the EFP near-body mesh which is approximately 70 million cells.

For the cases using the immersed-boundary representation of the EFP, the solver only required a surface grid to provide the ROAM solver a boundary definition. The surface grid sizing did not impact the solution. A new surface grid was generated using AFLR3 for this purpose.

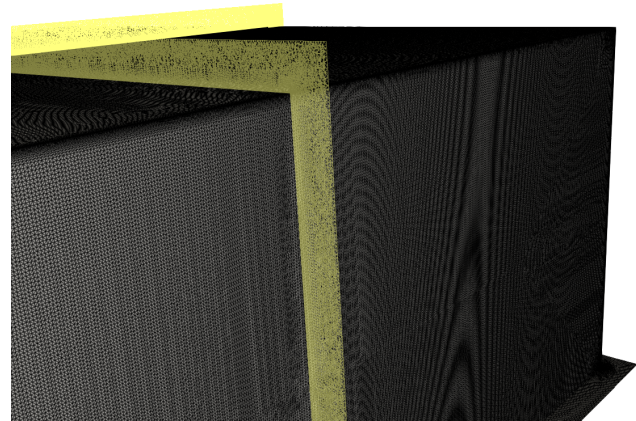


Figure 5: Unstructured mesh representation of the EFP.

The rotor blade structured-curvilinear OVERFLOW mesh was generated following the same best practice standards as described for the kCFD unstructured mesh. Each blade was resolved with three component overset meshes: one at the root, one along the main blade surface, and one at the tip. The main blade grid had 181 points around the airfoil, 175 points along the span, and 66 points in the wall-normal direction. Each blade mesh system had 5.3 million nodes - a total of 31.9 million nodes for all six rotor blades. Figure 6 provides a visual description of the blade mesh system. A slice of the combined mesh system is given in Fig. 7.

The immersed boundary and actuator line methods replace the corresponding meshes with a surface representation of the EFP and blades, respectively, so that the size of the mid-fidelity mesh incurs negligible computational cost compared to the volume grids. Also, switching between IBM and body-fitted meshes does not change the size of the off-body mesh, only which nodes are blanked. Therefore, the total mesh size varies from 621.5 million (with immersed boundary EFP and actuator lines and the aircraft closest to the EFP) to 1.1016 billion (with body-fitted EFP and meshed-blades and the aircraft furthest from the EFP) unique nodes/cells.

Numerical Solver Settings

In SAMCart, right-hand-side (RHS) terms were discretized using 5th-order central differences and 4th-order viscous dissipation. Left-hand-side (LHS) terms were discretized with a Lower-Upper Symmetric Gauss-Seidel (LUSGS) scheme. In OVERFLOW, RHS terms were discretized with 6th-order central differences and 6/2 dissipation, where the 4th- and 2nd-order dissipation constants were 0.2 and 2.0, respectively. LHS terms were discretized using a diagonalized Beam-Warming scalar pentadiagonal scheme with 4th-order

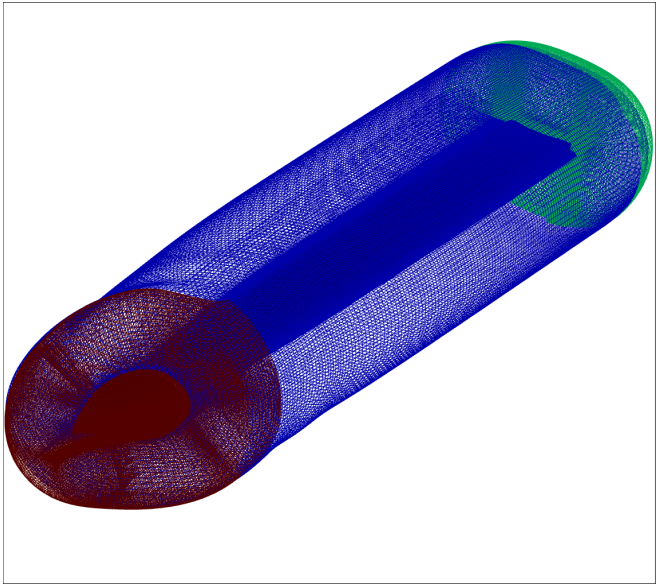


Figure 6: Structured multi-block mesh representation of the V-22 rotor blade.

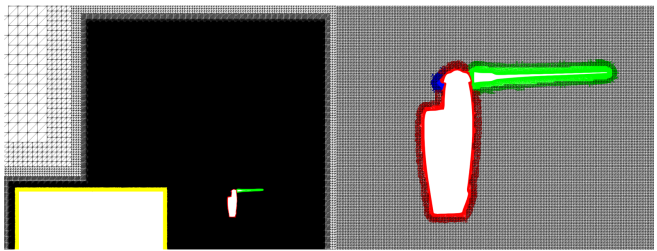


Figure 7: Slice through the left rotor showing the volume mesh system, including the EFP unstructured mesh (yellow), airframe unstructured mesh (red), rotor blade structured meshes (green), and Cartesian off-body mesh (black). Cropped to show detail.

dissipation. In kCFD, intra-cell linear gradients provide 2nd-order spatial accuracy. All solvers are 2nd-order accurate in time and use an implicit time-marching scheme with a time step corresponding to 0.5 degrees of rotor azimuth rotation in the meshed-blades approach and 1 degree in the actuator line approach. The number of subiterations varies by solver; SAMCart performs 7 subiterations when using meshed-blades and 9 for the actuator line approach, OVERFLOW performs 50 subiterations, and kCFD performs 20 subiterations. These values were chosen to provide approximately 2 orders of magnitude drop in the temporal residual. The impact of temporal residual drop on predicted aircraft performance was not quantified. To ensure the meshed-bladed approach had a solution which did not rely heavily on the solver and time step size, an isolated hover, $H = 20$ ft case was repeated using various near-body solvers (mStrand (Ref. 16), FUN3D (Ref. 17) and kCFD) for the fuselage and two different time step sizes ($\Delta t = 0.25^\circ$ and $\Delta t = 0.50^\circ$). There was no significant difference in the loads on the rotor among the different near-body solvers and time-step sizes. Therefore, since kCFD had the

fastest compute time per time-step, kCFD was used for the fuselage near-body solver with a $\Delta t = 0.50^\circ$ time step size.

To balance accuracy and speed for the actuator line/immersed boundary approach, the $1.3R$ -offset case was repeated using actuator line blades, immersed boundary airframe, and immersed boundary EFP with a $\Delta t = 0.50^\circ$ timestep size with 7 sub-iterations, $\Delta t = 1.0^\circ$ timestep size with 9 sub-iterations, and $\Delta t = 1.50^\circ$ timestep size with 11 sub-iterations. The rotor thrust and torque as well as the fuselage download varied only slightly for the three different cases. Therefore, a time step size of $\Delta t = 1.00^\circ$ with 9 sub-iterations was chosen for the actuator line/immersed boundary simulations as the balanced option between speed and technical risk.

Simulation Methodology

Because the initial conditions of a hover simulation are quiescent flow and the rotors instantaneously accelerate to full speed when the simulation begins, a large initial transient is generated. This transient is typically referred to as a starting vortex, since it manifests as a large, strong ring vortex generated by the rotors. While this vortex is near the aircraft, it significantly impacts the flow field and therefore the predicted aircraft performance. This is a well-known phenomenon in simulations of hovering rotors and is typically addressed by simulating many rotor revolutions until the starting vortex has dissipated or advected away before recording data. These “wake initialization” iterations add significant expense to the simulation, so a technique for accelerating this process that was designed and utilized in the sub-scale simulations (Ref. 7) was applied to this work. For the first 30 rotor revolutions of the simulation, the off-body grid was coarsened by one level (doubled cell size) in each refinement region and the number of subiterations was reduced to provide only one order of magnitude drop in the residual (4 for SAMCart, 10 for OVERFLOW, and 5 for kCFD). These compromises reduced the computational cost per iteration by at least 50% (more for the mid-fidelity simulations), saving at least 15% on the total computational cost of the entire simulation without impacting the final predictions.

The hovering aircraft was simulated for 100 total revolutions (30 wake initialization revolutions and 70 additional revolutions), independent of hover position, based on observed convergence of the rotor and fuselage loads. These loads were averaged over the last 30 revolutions for comparative analysis of aircraft performance. Simulations were performed on the HPCMP Distributed Supercomputing Resource Centers (DSRCs) “Narwhal” on 2,064 AMD 7H12 Rome Processors and “Warhawk” on 2,000 AMD 7H12 Rome processors. Due to the large mesh sizes, the processors were distributed among 24 128-core computing nodes (86 cores per node) on Narwhal and 16 128-core computing nodes (100 cores per node) on Warhawk so that each processor was granted a sufficient percentage of each node’s memory.

RESULTS

Aircraft Performance Prediction Results

Initial Comments: Before discussing the aircraft performance predictions, it is important to remember that there may be some discrepancy introduced due to the different methods for how each performance metric is measured in the computations and the flight test. In the flight test, torque was measured via the Mast Torque Sensing System (MTSS), whereas in the computations, the torque was calculated as the aerodynamic moment about the rotor axis integrated over the blade surfaces. In the flight test, rotor thrust had to be calibrated post-hoc as described in (Ref. 4). Jet thrust was estimated as an empirical function of engine shaft horsepower. Gross weight was calculated from empty gross weight, initial fuel weight, and integrated fuel burn at each test point (Ref. 4). Finally, download was derived via force balance of rotor thrust, exhaust jet thrust, and gross weight. In the computations, download was calculated as the vertical component of the integrated aerodynamic loads on the airframe surface (all modeled aircraft components excluding the rotor blades). Also, the flight test data was averaged over approximately 30-second records (206 rotor revolutions) for each hover location, whereas the computational results were averaged over the last 4.4 seconds (30 rotor revolutions) of a roughly 15-second (100-rotor-revolution) simulation.

Some sample plots of the convergence of torque and download in the computations are provided in Fig. 8 to contextualize the data provided in the following performance plots. Also displayed in these plots is the location where the wake initialization stage ended and the data stage began as well as the start of the averaging period. These plots clearly show that the wake initialization stage ended after the major effects from initial flow transients had subsided, and that the effect of additional transients from refining the off-body grid and increasing the solver subiterations was small, except when recirculation was already beginning to develop as was the case at $d/R = 1.5$. The choice of starting to average data after the 70th revolution was made to ensure that recirculating flow had fully developed. It can be seen in the convergence plots that it was appropriate to do so, as the nature of the mean value and unsteadiness in the performance metrics changed noticeably at or before this time as recirculation fully develops at each hover location. However, the variability of torque and download within these last 30 revs indicates that many more revolutions of data would be required to eliminate any statistical sampling error from the computational results. Due to the already-high cost of these simulations, this potential source of error was not addressed.

EFP-Centerline-Aligned Sweep of Rotor Tip Clearance: Figure 9 compares mean rotor torque and airframe download between the high-fidelity and mid-fidelity simulations for a sweep of tip clearance at a hover height (to the rotor hubs) of 2.0R and with the aircraft centerline aligned with the EFP centerline. Experimental and computational torque data are normalized by their respective OGE values to correct for mod-

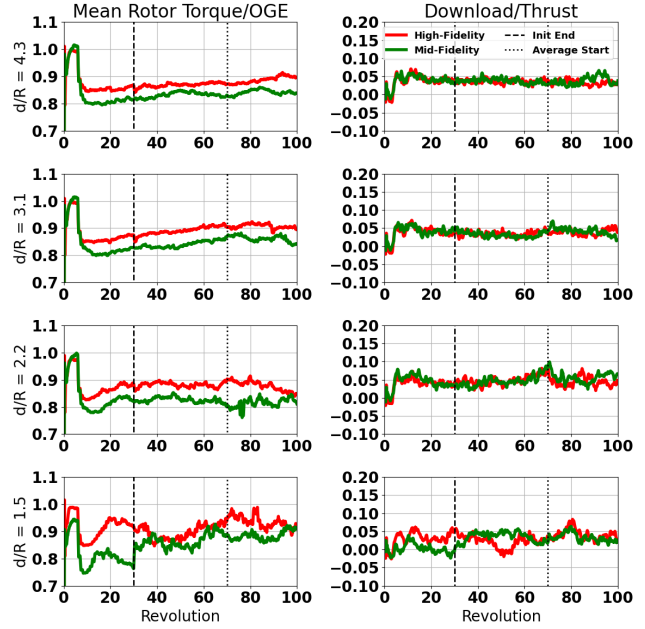


Figure 8: Time histories of mean rotor torque and airframe download during the computational simulations of a sweep of wall distance at a constant hub height above ground of $h/R = 2.0$.

eling uncertainties and to focus on physical trends with varying relative position of the aircraft and EFP. Download was normalized by the total rotor thrust at each test point. In the torque plot, there is an interesting feature in the flight test data where the torque dropped at $d/R = 2.1$, then rose sharply at $d/R = 1.5$. Both simulations captured this trend. The high fidelity simulation tended to overpredict the power until the closest tip clearance, where it agreed very well with the flight test data, while the mid-fidelity simulation underpredicted the rotor torque. Both models overpredicted download in ground effect at this aircraft height, even away from the EFP, but did agree with the flight test data that download is relatively constant with rotor tip clearance, although there was a small uptick in download at $d/R = 1.5$ that was not captured by the computations. The high-fidelity and mid-fidelity simulations predicted the flight test torque within 3.4% and 3.2% of OGE torque, respectively. They predicted download within 3.2% and 3.8% of thrust compared to the flight test data, respectively.

Because the fluid dynamics in these flight conditions are so unsteady, the provided performance plots also include error bars indicating the standard deviations in the data for both the flight test and the computational predictions. These standard deviations were calculated after filtering out oscillations above the rotor frequency to focus on low-frequency unsteadiness that would drive pilot workload and aircraft performance. As expected, the unsteadiness rose as the aircraft approached the EFP, which is consistent with pilot comments during the flight test. The unsteadiness in the flight test data is higher than observed in the CFD predictions, which is attributed to

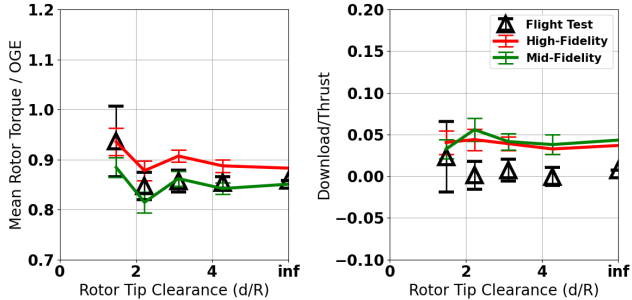


Figure 9: Comparison between mean rotor torque and airframe download flight test data and predictions from high- and mid-fidelity simulations for a sweep of rotor tip clearance at a constant hover height of 2.0R to the rotor hubs with the aircraft and EFP centerlines aligned. Error bars indicate standard deviation of 1/rev-filtered signal

additional low frequency variation induced by the pilot response to the aerodynamic unsteadiness that is not modeled in the CFD. Further investigation into whether coupling the CFD to flight dynamics software with a pilot model better captures this variation is currently underway.

EFP-Portside-Aligned Sweep of Rotor Tip Clearance: Figure 10 provides similar performance data, but with the aircraft centerline aligned with the port edge of the EFP. Left and Right rotor torque trends are also provided. Here there was a more monotonic increase in mean rotor torque with decreasing tip clearance that was well-captured by the high-fidelity simulations and somewhat underpredicted by the mid-fidelity simulations. Airframe download was negligibly impacted by the change in modeling fidelity, and was again somewhat over-predicted in the computations, although for this sweep, the increase in download with lower tip clearance was well captured. In the individual rotor data, the flight test measured a more severe increase in torque for the right rotor than for the left rotor as the aircraft approached the EFP, whereas the opposite was true for the computational predictions. The mid-fidelity prediction of right rotor torque at $d/R = 1.5$ was significantly different than the flight test data, underpredicting it by 10% of OGE torque. This is a consistent finding with the sub-scale study, where IBM fundamentally altered the predicted physics of flow recirculation and introduced large errors for small distances between the rotor and the obstacle. The high-fidelity and mid-fidelity simulations predicted the mean flight test torque within 1.8% and 5.1% of OGE torque, respectively, and predicted download within 2.4% and 2.8% of thrust, respectively, compared to the flight test data. For left rotor torque, the respective error for the high- and mid-fidelity simulations was 2.9% and 5.3% of OGE torque, and for the right rotor, it was 1.8% and 5.4%, respectively.

EFP-Centerline-Aligned Sweep of Rotor Hub Height Above-Ground: Figure 11 compares mean rotor torque and airframe download between the high-fidelity and mid-fidelity

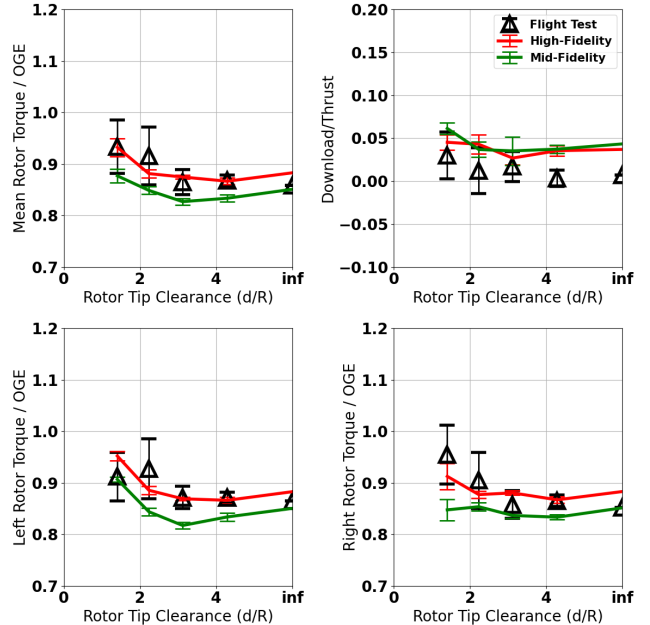


Figure 10: Comparison between mean rotor torque and airframe download flight test data and predictions from high- and mid-fidelity simulations for a sweep of rotor tip clearance at a constant hover height of 2.0R to the rotor hubs with the aircraft centerline and EFP port edge aligned. Error bars indicate standard deviation of 1/rev-filtered signal

simulations for a sweep of hover height at a tip clearance of 1.3R and the aircraft centerline aligned with the EFP centerline. Because there were now two competing effects on rotor torque, namely ground effect and recirculation, isolated hover performance data taken with the aircraft away from the EFP is provided in the top row for reference. Performance data taken near the EFP is in the middle row, then the delta between the two is provided in the bottom row. This bottom row should isolate the performance impact of the EFP at the different heights from the expected performance impacts of ground effect. Because the ground-effect predictions were discussed extensively in Ref. 4, the current discussion will primarily focus on the figures in the bottom row. Here it can be seen that both the mid-fidelity and high-fidelity simulations captured the peak in recirculation-induced torque when the rotors were 2.0R above the ground, which corresponds approximately with the height of the EFP. The download predictions were less consistent with the flight test data, influenced largely by the mismatch in download predictions away from the EFP in ground effect. This may be attributed to a number of factors, including perhaps a need for better turbulence modeling, a more refined airframe mesh, more accurate modeling of the airframe geometry details, or modeling the ground plane as a viscous surface. Here, the high-fidelity and mid-fidelity predictions of overall torque (middle row) were within 1.8% and 2.9% of OGE torque, respectively. The download predictions were within 2.7% and 1.0% of thrust, respectively.

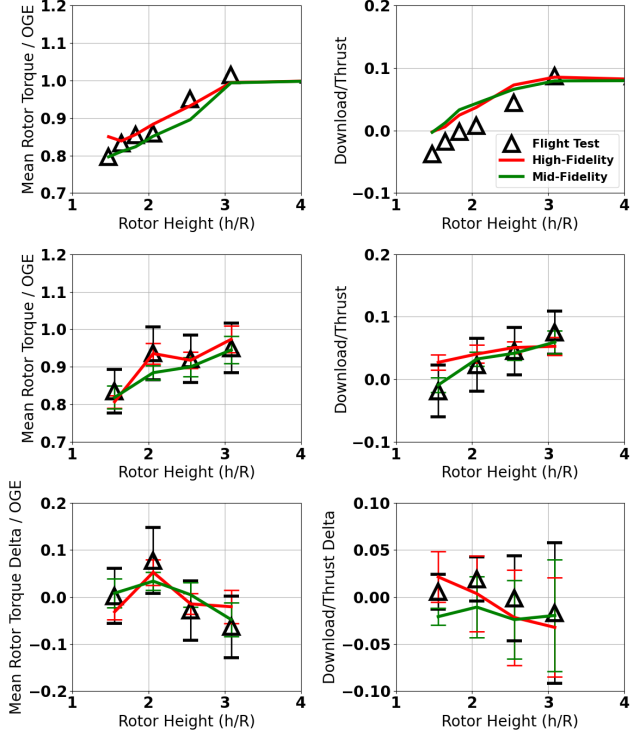


Figure 11: Comparison between mean rotor torque and airframe download flight test data and predictions from high- and mid-fidelity simulations for a sweep of rotor hub height at a constant tip clearance of 1.3R with the aircraft and EFP centerlines aligned. Isolated hover data (top), EFP data (middle), and the deltas between them (bottom) are provided. Error bars indicate standard deviation of 1/rev-filtered signal

EFP-Portside-Aligned Sweep of Rotor Hub Height Above-Ground: Figure 12 provides similar plots, but with the aircraft centerline aligned with the port edge of the EFP. Here, the delta-torque maximum at $d/R = 2.0$ was less pronounced in the flight test data, and is not apparent in the computational predictions. Overall, the influence of recirculation on torque appears to be relatively constant with rotor height in this particular alignment with the EFP. Download predictions were more consistent with the flight test data, where the mean download deltas were relatively constant up to $h/R = 2.6$, and then reversed sign at $h/R = 3.2$. The computations predicted this sign reversal in recirculation-induced download at much lower heights, with both fidelity levels agreeing fairly well with each other. For this sweep, the high-fidelity and mid-fidelity predictions of overall mean torque were within 4.5% and 7.9% of OGE torque, and within 1.8% and 2.3% of thrust compared to the flight test, respectively. Figure 13 breaks out the left and right rotor torque predictions. As observed in the sweep of tip clearance, the mid-fidelity model underpredicted right rotor torque by about 10%, as the rotor is very close to the EFP. For left rotor torque, the respective error for the high- and mid-fidelity simulations was 4.0% and 5.4% of OGE torque, and for the right rotor, it was 5.4% and 10.4%, respectively.

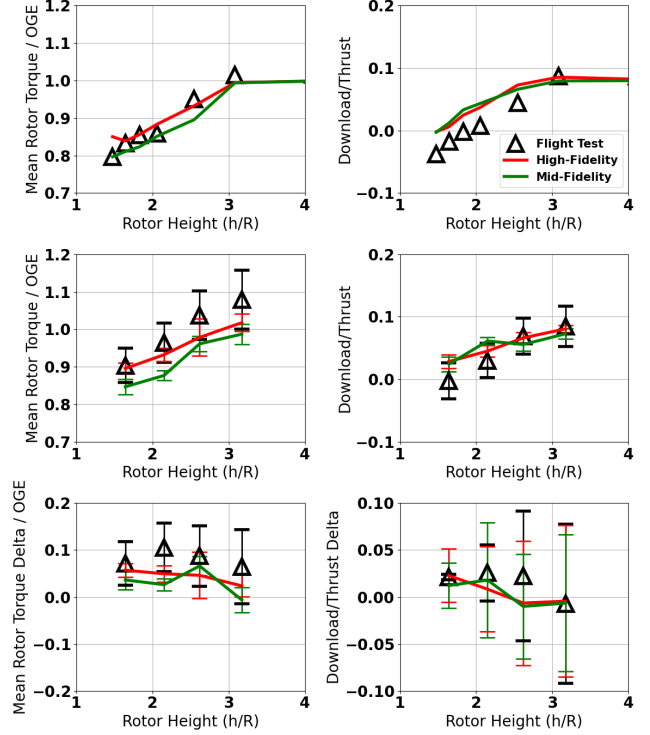


Figure 12: Comparison between mean rotor torque and airframe download flight test data and predictions from high- and mid-fidelity simulations for a sweep of rotor hub height at a constant tip clearance of 1.3R with the aircraft centerline and EFP port edge aligned. Isolated hover data (top), EFP data (middle), and the deltas between them (bottom) are provided. Error bars indicate standard deviation of 1/rev-filtered signal

Cost vs. Fidelity Tradeoff: Table 3 summarizes the accuracy and cost of the various computational approaches. The mid-fidelity simulations blades required approximately 83% fewer CPU-hours to complete each simulation (6X speedup) compared to the high-fidelity simulations, due primarily to the higher time step (2X) and the reduction in the computational mesh size. The mesh size was reduced by 31.9 million structured nodes from using actuator lines instead of meshed blades, and by 70 million unstructured cells from using IBM instead of a body-fitted mesh for the EFP. Unstructured cells are typically more expensive to compute, though because the structured cells were on the only moving bodies, their elimination also eliminated the need to re-compute domain connectivity every iteration, so it is unclear which reduction was more impactful on computational cost. Considering the small difference in performance predictions with respect to the high-fidelity approach, it can be concluded that mid-fidelity models applied in this work can be a cost-effective solution for predicting integrated aircraft performance impacts due to ground obstacle interactions for most applications. The validity of such an approach is dependent upon the accuracy requirements of the particular use case. Improvements to the actuator line and immersed boundary methods may improve the torque predictions further, and investigating this possibility is

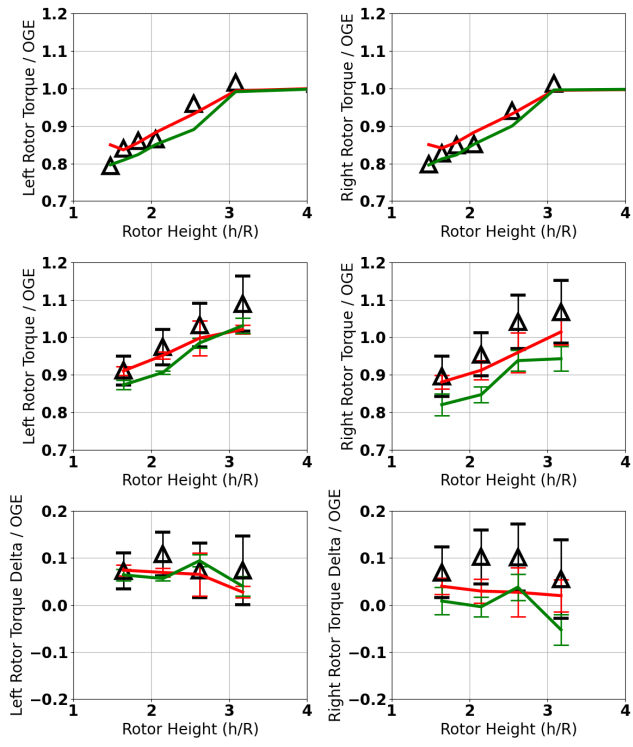


Figure 13: Comparison between left and right rotor torque flight test data and predictions from high- and mid-fidelity simulations for a sweep of rotor hub height at a constant tip clearance of 1.3R with the aircraft centerline and EFP port edge aligned. Isolated hover data (top), EFP data (middle), and the deltas between them (bottom) are provided. Error bars indicate standard deviation of 1/rev-filtered signal

planned as future work.

Flow Visualization Analysis

EFP-Centerline-Aligned Sweep of Rotor Tip Clearance:

In Fig. 14, one of the primary driving influences of these flow fields can be observed at $d/R = 4.3$, namely the strong wall jet resulting from the interaction between the downwash of the left and right rotor. It is this wall jet that impinges on the EFP and is directed upward. Even with the V-22 at this furthest distance, this upwash recirculated towards the aircraft and was reingested into the rotors. As the aircraft approached the EFP, the recirculating flow path contracted and the reingested flow accelerated above the aircraft. The wall jet along the ground in front of the aircraft weakened as the EFP interfered with the V-22 outwash profile, particularly at $d/R = 1.5$. There are

Table 3: Summary of mean rotor torque prediction accuracy as well as computational expense.

Fidelity	Q Err. (% of OGE)	DL Err. (% of Thrust)	CPU-hours/rev
High	3.1%	2.6%	23,700
Mid	5.2%	2.6%	4,000

only subtle differences observed in the flow fields between the two modeling fidelities, the most apparent of which is the reduction of the flow velocity directly over the wing box as a result of the weaker tip vortices generated by the actuator line model creating a less turbulent fountain effect. The difference in rotor modeling is the more likely driving factor in the difference in download trends predicted by the two models, as opposed to the immersed boundary modeling of the EFP.

Focusing on the left rotor system in Fig. 15, the impact of modeling fidelity on the flow field is somewhat more apparent, with higher peak velocities in the phase-averaged velocity magnitude field predicted by the high-fidelity model due to the stronger tip vortices. Once the vortex structures in the rotor wake are thoroughly mixed as the wake propagates towards the EFP, the modeling differences become less apparent. When the rotor wake impinges on the EFP, the immersed boundary method appears to have reduced the flow velocity more than the body-fitted EFP grid, resulting in a tighter recirculating flow path at all but the furthest tip clearance. This observation agrees with those from the model-scale V-22 recirculation computational study (Ref. 4), where it was concluded that an inviscid or wall-modeled immersed boundary is more appropriate than a stair-step immersed boundary for these recirculation applications. It is likely for this reason that the mid-fidelity model predicted slightly lower torque during recirculation than the high-fidelity model.

The spanwise-vorticity fields provided in Fig. 16 give a very clear picture of the difference in tip-vortex modeling fidelity between the two rotor models, and highlight the level of turbulence present in the recirculation vortex. It is hypothesized that this turbulence, not just the higher inflow velocity, is one of the driving factors of rotor performance loss during recirculation. It can at least be observed that when this turbulent inflow was ingested, the normally coherent vortex structures (tip vortices and vortex sheet) broke down almost immediately. This turbulence can be somewhat more directly observed in the instantaneous three-dimensional flow visualization provided in Fig. 17. In these images one can get a sense of the unsteady, asymmetrical, and turbulent flow field that the aircraft was operating within.

EFP-Portside-Aligned Sweep of Rotor Tip Clearance:

When the aircraft was aligned with the port edge of the EFP, the observed recirculation vortex in Fig. 18 appears to have been weaker than when the aircraft was aligned with the EFP centerline. The same observation holds when looking at a slice of the flow field through the right rotor in Fig. 19. There also appears to have been much less turbulence being ingested when the tip clearance was 2.2R compared to the same centerline-aligned cases (Fig. 20). This correlates with the different trends in rotor power between the centerline and port-aligned wall distance sweeps. These phenomena can be contextualized by viewing the three-dimensional flow field in Fig. 20, where it is much clearer that at tip clearances greater than 1.5R, the forward outwash jet was being heavily deflected starboard away from the aircraft. The reason for this starboard deflection of the recirculating outwash jet is unclear,

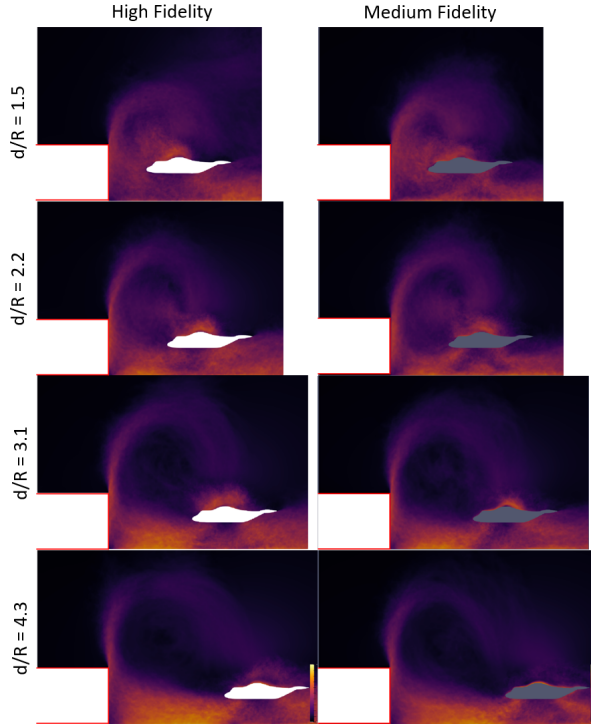


Figure 14: Phase-averaged velocity magnitude contours on a plane through the V-22 centerline for an EFP-centerline-aligned sweep of tip clearance with the high-fidelity and mid-fidelity models.

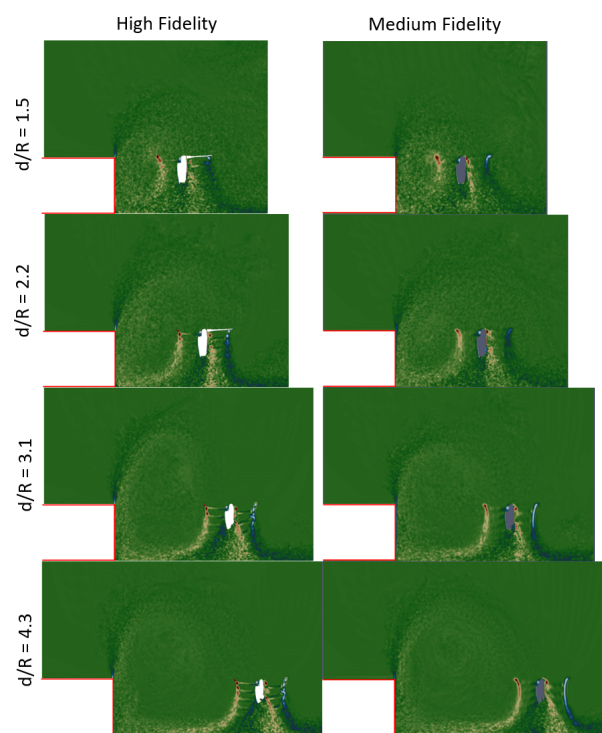


Figure 16: Phase-averaged Y-vorticity contours on a plane through the V-22 left rotor hub for an EFP-centerline-aligned sweep of tip clearance with the high-fidelity and mid-fidelity models.

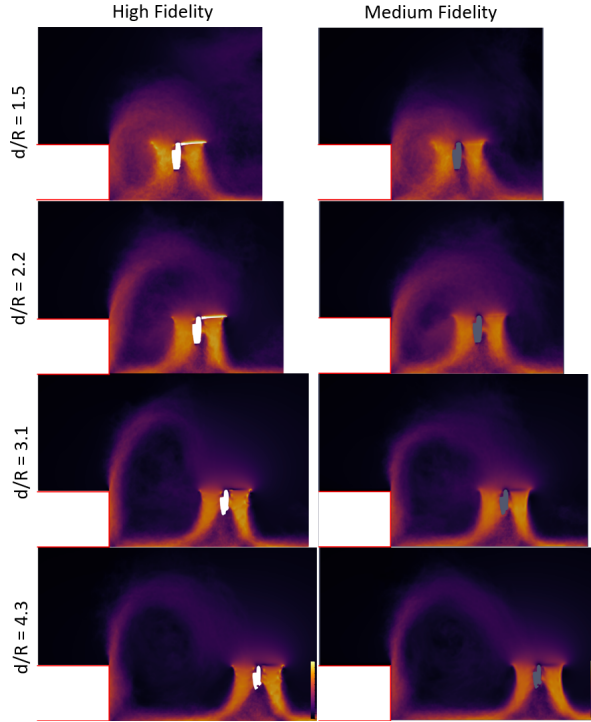


Figure 15: Phase-averaged velocity magnitude contours on a plane through the V-22 left rotor hub for an EFP-centerline-aligned sweep of tip clearance with the high-fidelity and mid-fidelity models.

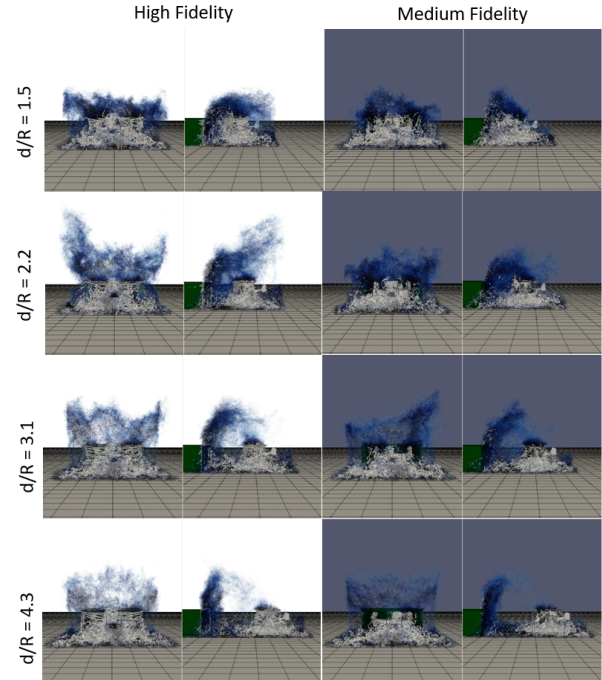


Figure 17: Instantaneous vorticity isosurfaces for an EFP-centerline-aligned sweep of tip clearance with the high-fidelity and mid-fidelity models. The lower-level isosurface is colored by and has its opacity based on velocity magnitude.

but it is hypothesized that there was a port/starboard asymmetry in static pressure along the port edge of the EFP caused by the bifurcation of the V-22 forward outwash jet.

EFP-Centerline-Aligned Sweep of Rotor Hub Height

Above-Ground: From the flow visualization thus far, it is apparent that the height of the EFP played a significant role in the development of the recirculation vortex. Figure 22 demonstrates that, even if the rotors were well below the height of the obstacle, the outwash jet only began recirculating when it reached the top of the EFP. This means that, despite the higher velocity of the wall jet at lower heights, flow recirculation can actually be less severe. When the rotor was aligned with the top of the EFP, shown most clearly in Fig. 23, the speed of the recirculation was highest, which is particularly apparent in the high-fidelity results. This corresponds to an upward “kink” in the rotor torque that was only predicted by the high-fidelity simulation. It is important to remember that there are two competing effects on the rotor torque: recirculation and ground effect. It was only at this particular point that the recirculation overcame ground effect to increase torque relative to the next highest point. Figure 24 also shows the least coherent vortex sheet at $h/R = 2.0$ among the high-fidelity predictions. Most of the mid-fidelity predictions did not show any coherent vortex sheet due to the actuator-line modeling of the rotor. Comparing the mid-fidelity and high-fidelity velocity magnitude contours at $h/R = 1.6$ in Figs. 22 and 23, there was an interesting flip in the lateral profile of the recirculation. The mid-fidelity model predicted strong recirculation through the left rotor disk and an outwash jet that was primarily blown up and away from the aircraft centerline, whereas the high-fidelity model predicted some recirculation at the aircraft centerline with the outwash primarily blown up and away from the left rotor. This can be understood by observing Fig. 25, where, in these instantaneous snapshots, the recirculating outwash jet was sometimes bifurcated and sometimes was not. Animations of the flow field show that these two states were present to varying degrees in every simulation, and there may be an element of chance as to which one dominated the phase-averaged visualization due to the short 100-rev simulation time.

EFP-Portside-Aligned Sweep of Rotor Hub Height

Above-Ground: For the port-aligned sweep of rotor height, the performance predictions between the two modeling fidelity levels were very similar, and comparing the flow fields provided in Figs. 26-29 reveals similar agreement. The decreased peak in recirculation-induced torque at $h/R = 2.0$ corresponds with less pronounced recirculation through the rotor system compared to the EFP-centerline-aligned sweep of rotor height. One can see in the three-dimensional flow visualization that the region of recirculating flow remained mostly unchanged with varying height except at the lowest rotor height, where the starboard-skewed outwash jet once again becomes apparent.

Inflow Analysis

In an attempt to investigate the aerodynamic mechanisms of rotor performance changes in recirculating flow fields, analysis of the rotor inflow was performed based on the phase-averaged flow field slices. The inflow was measured by inspecting the velocity vector along a line in the flow field corresponding to where the right blade quarter-chord would be positioned when pointing towards the nose of the aircraft ($\psi = 180^\circ$). Since the slices were phase locked with the blades in the opposite orientation, there was no blade present at this position in the phase averaged flow fields. This velocity vector was converted into inflow angle (θ_{inflow}) by adding the local blade section’s rotational velocity (Ωr) to the in-rotor-plane fluid velocity ($-v$) and taking the negative arctangent of the in-rotor-plane and vertical (w) components of fluid velocity:

$$\theta_{inflow} = -\arctan(w/(\Omega r - v)) \quad (1)$$

An example image showing the inflow extraction location and the inflow calculated over a flow slice without the EFP is provided in Fig. 30. An average inflow angle was calculated by averaging the inflow angle from 50%-90% radius in order to focus on inflow differences over the working section of the blade and prevent contamination from any inaccuracies in inflow extraction location and variabilities in the tip vortex location that can artificially magnify measured inflow differences at the root and tip of the blade.

The baseline blade performance in non-recirculating flow was acquired by measuring the inflow at various hover heights above the ground in simulations without the EFP. With this, the baseline effect of angle of attack (α) on rotor thrust could be established. Deltas in rotor thrust (ΔT) and deltas in angle of attack ($\Delta\alpha$) were calculated relative to the OGE data, with changes in instantaneous blade pitch and inflow at $\psi = 180^\circ$ used to calculate deltas in angle of attack. The relationship is primarily linear (see Fig. 31) between a change in angle of attack and a change in rotor thrust, which is expected since it is well known that ground effect increases rotor performance due to reduced inflow. Therefore, this relationship was approximated with a least-squares fit linear function with a slope of about 0.021 pounds of thrust per pound of gross weight per degree change in angle of attack.

This function was used to test whether aircraft performance loss during recirculation was caused primarily by increased inflow due to the recirculating rotor downwash, or if the actual aerodynamic performance of the blades was being degraded by the turbulence being ingested into the rotor. If the former is true, then one would expect to see a similar relationship between delta thrust and delta angle of attack for the simulations of the aircraft near the EFP as that observed in simulations without the EFP. To measure this agreement, a metric called “thrust performance deficit” (TPD) was devised with the following definition:

$$TPD = 0.021\Delta\alpha - \Delta T/GW \quad (2)$$

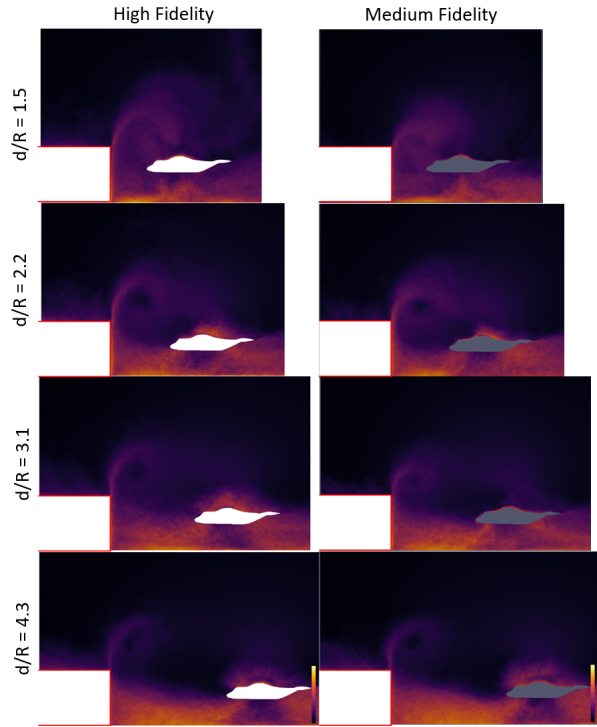


Figure 18: Phase-averaged velocity magnitude contours on a plane through the V-22 centerline for an EFP-portside-aligned sweep of tip clearance with the high-fidelity and mid-fidelity models.

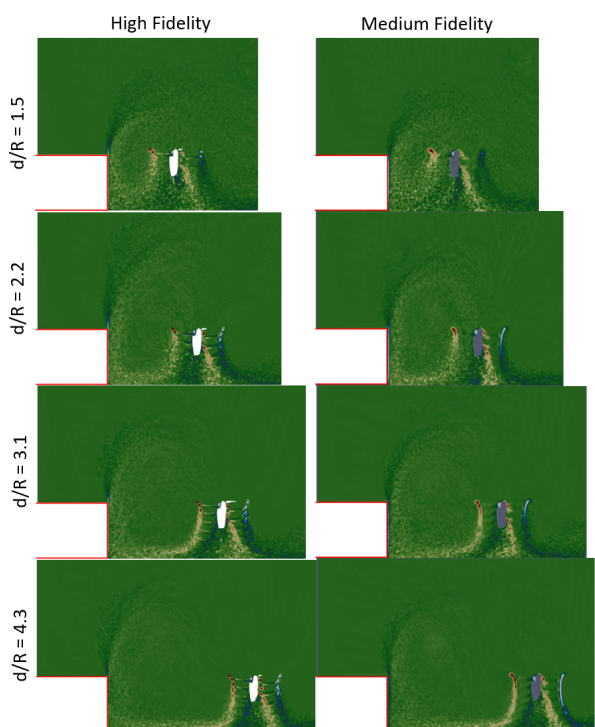


Figure 20: Phase-averaged Y-vorticity contours on a plane through the V-22 right rotor hub for an EFP-portside-aligned sweep of tip clearance with the high-fidelity and mid-fidelity models.

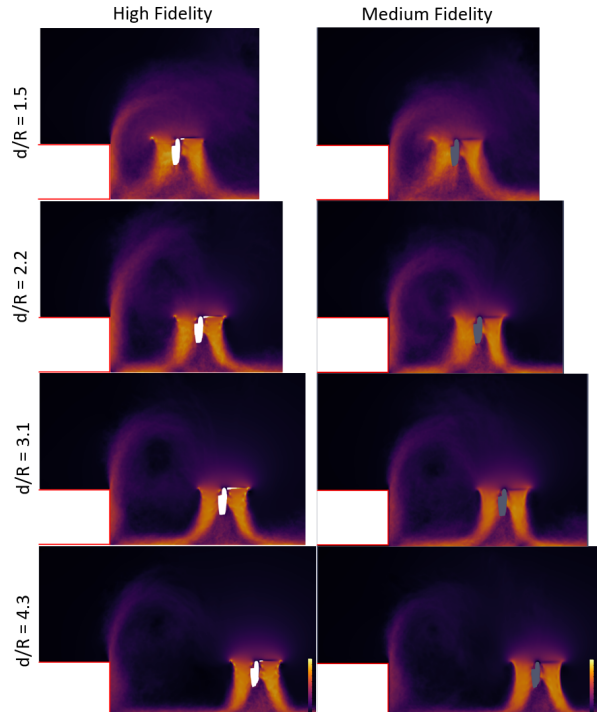


Figure 19: Phase-averaged velocity magnitude contours on a plane through the V-22 right rotor hub for an EFP-portside-aligned sweep of tip clearance with the high-fidelity and mid-fidelity models.

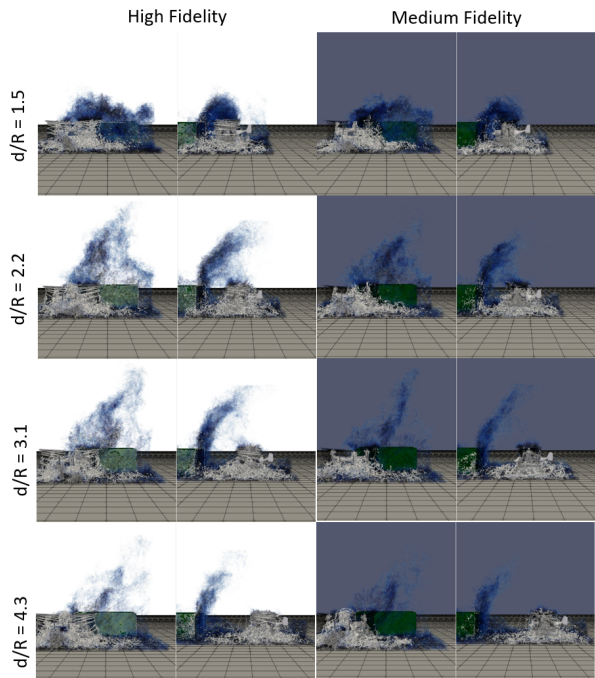


Figure 21: Instantaneous vorticity isosurfaces for an EFP-portside-aligned sweep of tip clearance with the high-fidelity and mid-fidelity models. The lower-level isosurface is colored by and has its opacity based on velocity magnitude.

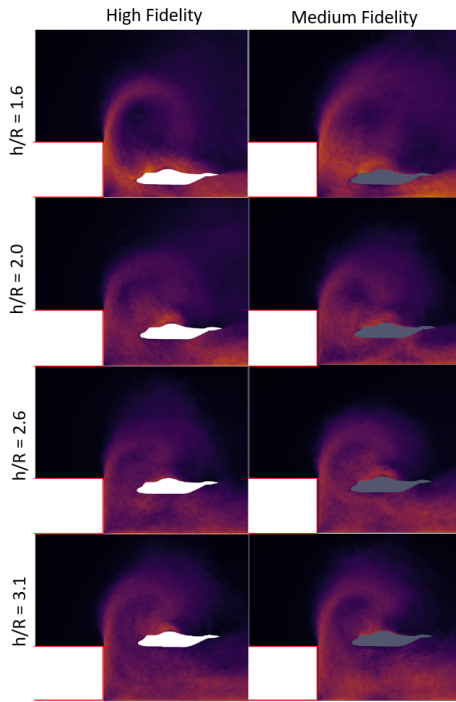


Figure 22: Phase-averaged velocity magnitude contours on a plane through the V-22 centerline for an EFP-centerline-aligned sweep of rotor height with the high-fidelity and mid-fidelity models.

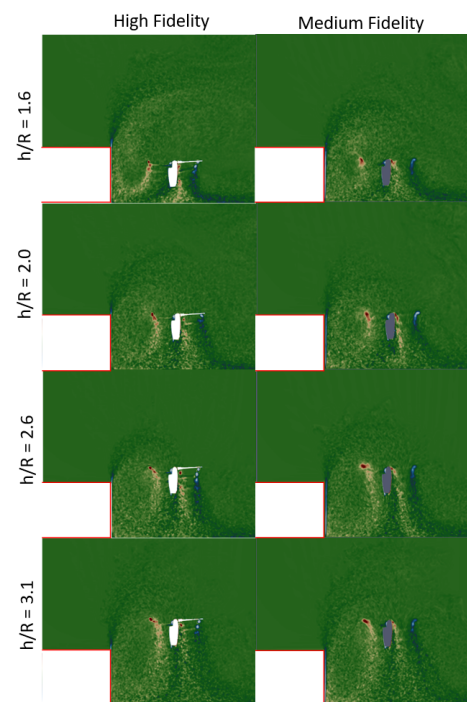


Figure 24: Phase-averaged Y-vorticity contours on a plane through the V-22 left rotor hub for an EFP-centerline-aligned sweep of rotor height with the high-fidelity and mid-fidelity models.

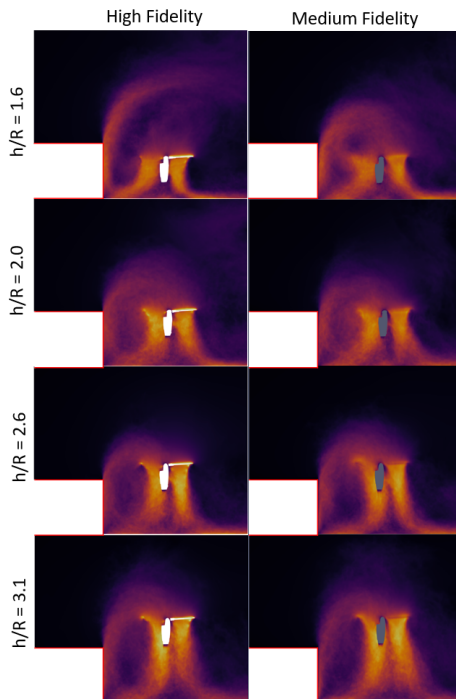


Figure 23: Phase-averaged velocity magnitude contours on a plane through the V-22 left rotor hub for an EFP-centerline-aligned sweep of rotor height with the high-fidelity and mid-fidelity models.

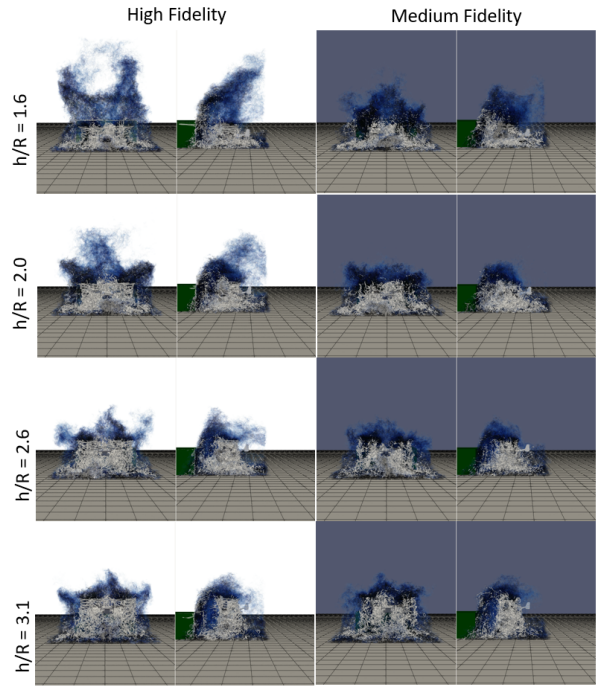


Figure 25: Instantaneous vorticity isosurfaces for an EFP-centerline-aligned sweep of rotor height with the high-fidelity and mid-fidelity models. The lower-level isosurface is colored by and has its opacity based on velocity magnitude.

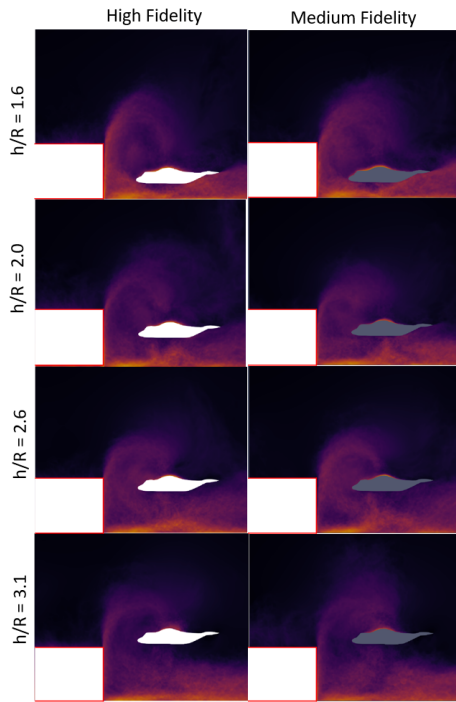


Figure 26: Phase-averaged velocity magnitude contours on a plane through the V-22 centerline for an EFP-portside-aligned sweep of rotor height with the high-fidelity and mid-fidelity models.

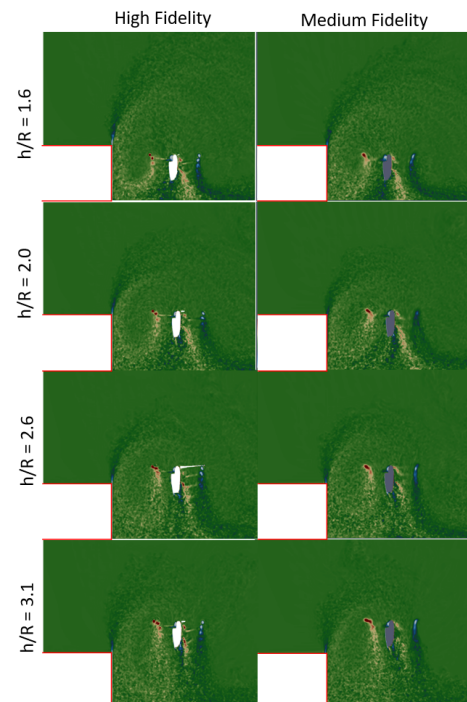


Figure 28: Phase-averaged Y-vorticity contours on a plane through the V-22 right rotor hub for an EFP-portside-aligned sweep of rotor height with the high-fidelity and mid-fidelity models.

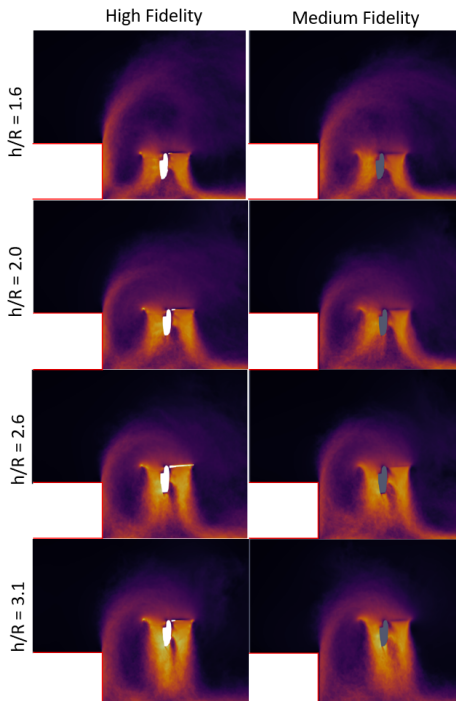


Figure 27: Phase-averaged velocity magnitude contours on a plane through the V-22 right rotor hub for an EFP-portside-aligned sweep of rotor height with the high-fidelity and mid-fidelity models.

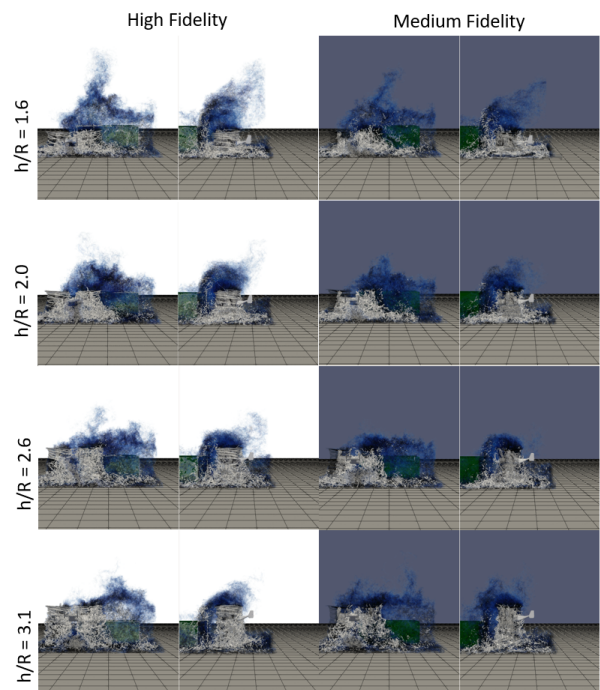


Figure 29: Instantaneous vorticity isosurfaces for an EFP-portside-aligned sweep of rotor height with the high-fidelity and mid-fidelity models. The lower-level isosurface is colored by and has its opacity based on velocity magnitude.

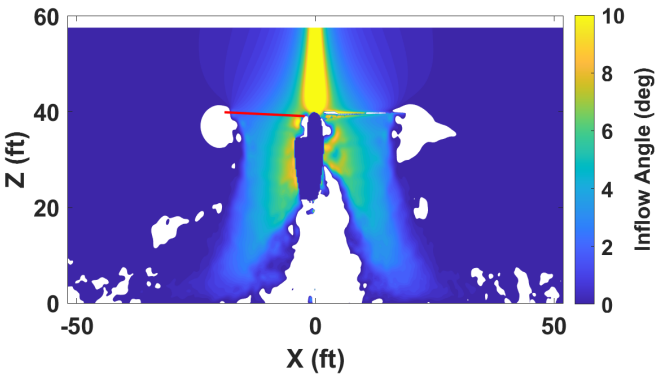


Figure 30: Phase-averaged inflow field for the right V-22 rotor in hover at a 20ft wheel height predicted with the high-fidelity model. Inflow extraction line shown in red. White regions indicate upwash.

This simply compares the measured thrust delta with respect to operations OGE when operating near the EFP, normalized by gross weight (GW), with what would be expected based on the measured delta in angle of attack. If the TPD is always small, then aircraft performance loss can be explained primarily by increased inflow due to recirculation, otherwise, there is some other effect at play. Inspecting TPD for test points in the EFP-centerline-aligned tip-clearance sweep at $d/R = 4.3, 2.2$, and 1.5 in Fig. 32, one can see that there was a clear change in TPD with the onset of recirculation. Inflow data for $d/R = 3.1$ was not available due to an archiving error. More accurate and thorough analysis is therefore required to establish a clear causal factor for recirculation-induced aircraft performance loss aside from simple changes in inflow magnitude. As mentioned previously, it is currently speculated that the mechanism is related to the turbulence ingested into the rotor reducing the aerodynamic performance of the blades, but the current analysis was not sophisticated enough to make any definite conclusions. Further research into this hypothesis is necessary.

CONCLUSIONS

This work investigated modeling requirements for replicating tiltrotor flight test data in hover near a ground obstacle with CFD. The test data were analyzed and corrected to enable accurate representation of the test conditions in the computation. The processed test data were translated to simulation inputs through an automated pipeline.

It was determined that a mid-fidelity representation of the rotors and obstacle is sufficient to predict trends in rotor performance with varying hover location relative to the obstacle. The error in performance predictions relative to the flight test was on the same order as the accuracy of the high-fidelity simulations. The mid-fidelity approach provided a 6X speedup in the computations. The computational methods were generally able to predict trends in aircraft performance with varying position relative to the obstacle, with some biases during certain sweeps for both levels of fidelity. The computations

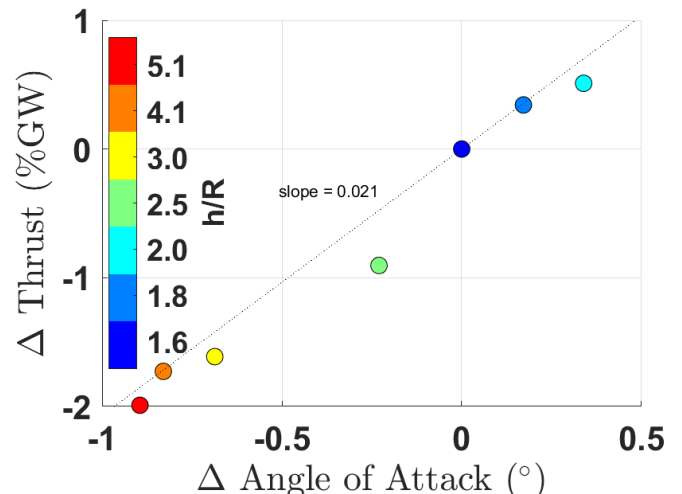


Figure 31: High-fidelity prediction of delta-thrust induced by ground effect as a function of change in blade angle of attack, baselined to OGE prediction. The marker colors from blue to red correspond to increasing rotor height.

also underpredicted variance in aircraft performance near the obstacle, which is attributed to the lack of flight dynamics and pilot-model coupling. These results establish confidence in applying both actuator lines and meshed blades to these interactional flow fields for the purpose of investigating the physics of aircraft performance loss during operations near a ground obstacle, and further motivate ongoing work to couple detailed flight dynamics models of Navy aircraft to Helios simulations.

In analyzing images of the flow field, the physical features of recirculating flows are established at various aircraft positions relative to the obstacle. Many of these features are expected to be unique for transverse-rotor aircraft, e.g. tiltrotor aircraft. Additionally, it was established that aircraft performance loss

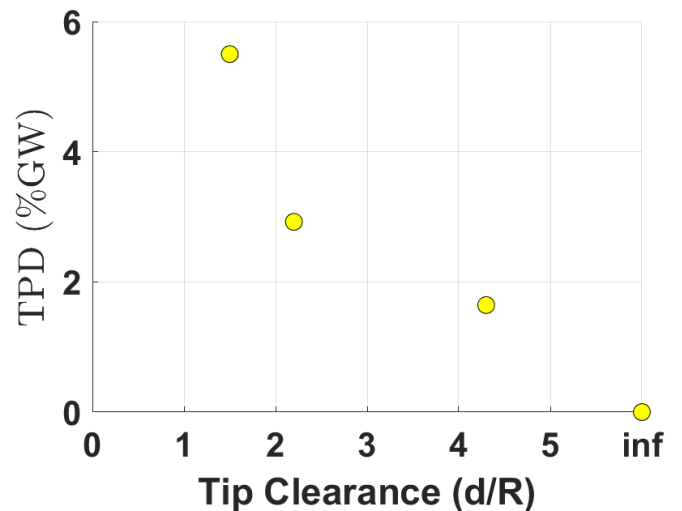


Figure 32: V-22 right rotor thrust performance deficit (TPD) calculated at various distances from the EFP by the high-fidelity model. All data points are at $h/R = 2.0$.

cannot be entirely explained by an increase in inflow velocity through the rotor system during recirculation. Further research is required into whether it can be attributed to increased turbulence in the rotor inflow due to the re-ingested wake.

ACKNOWLEDGEMENTS

This work is funded under the Naval Innovative Science & Engineering (NISE) program project number 219BAR-22-004. Computational time was provided by the HPCMP through the “Modeling & Simulation for Air/Ship Integration (A/SI) Program Support” Frontier Project. Thanks are given to Susan Polsky, Buvaneswari Jayaraman, Mark Silva, and the Helios support and development staff for their guidance and assistance during the execution of this work. All opinions expressed herein are those of the authors and are not endorsed by the U.S. Government.

REFERENCES

1. Lumsden, R. B., and Wilkinson, C. H., “Challenges at the Helicopter-Ship Dynamic Interface,” Proceedings of the 24th European Rotorcraft Forum, Marseilles, France, Sept. 15–17, 1998.
2. Advani, S. K., and Wilkinson, C. H., “Dynamic Interface Modelling and Simulation —A Unique Challenge,” Proceedings of the Royal Aeronautical Society Conference on Helicopter Flight Simulation, London, United Kingdom, Nov. 7–9, 2001.
3. Pritchard, J. A., and Findlay, D., “DIVE Overview,” AIAA Paper 2021-2478, AIAA Aviation 2021 Forum, Virtual Event, Jul. 28, 2021. DOI: 10.2514/6.2021-2478.
4. Moushegian, A. M., Farish, D. . M ., Hayden, E. W., and Bodling, A. L., “Investigation of Modeling Approaches to High-Fidelity Computational Predictions of Tiltrotor Hover Aeromechanics,” VFS Paper F-0080-2024-1089, VFS’s 80th Annual Forum & Technology Display, Montréal, Québec, Canada, May 7–9, 2024. DOI: 10.4050/F-0080-2024-1089.
5. Silva, M. J., Schatzman, D., and Ramasamy, M., “Sub-Scale Investigation of Coupled Rotor/ Upwind Ship Aerodynamic Interactions,” VFS Paper sm-2024-Aeromechanics-052-2-05-Silva, VFS’s 6th Decennial Aeromechanics Specialists’ Conference, Santa Clara, CA, Feb. 6–8, 2024.
6. Silva, M. J., Hromisin, S., Corbett, M., Graybeal, N., Cato, S., Ralston, J., Prevost, R., and Gray, C., “Model-Scale Investigation of Tiltrotor Low-Speed Obstacle-Induced Downwash Recirculation,” Paper VFS 2023-0046, Vertical Flight Society’s 79th annual Forum and Technology Display, West Palm Beach, FL, June 16–18, 2023.
7. Moushegian, A. M., and Yikloon, L., “Investigation of Computational Modeling Approaches to Prediction of Tiltrotor / Obstacle Interactions at Model Scale,” VFS Paper sm-2024-Aeromechanics-031-1-07-Moushegian, VFS’s 6th Decennial Aeromechanics Specialists’ Conference, Feb. 6–8, 2024.
8. Silva, M. J., Hayden, E. W., Myers, L. M., Tritschler, J. K., and Holder, J. M., “Full-Scale Investigation of Rotor/Obstacle Interactions Using an Elevated Fixed Platform,” VFS Paper F-0078-2022-17628, VFS’s 78th Annual Forum & Technology Display, Ft. Worth, TX, May 10–12, 2022. DOI: 10.4050/F-0078-2022-17628.
9. Narducci, R., Liu, J., Wells, A. J., Mobley, F. M., and Mayer, R. J., “CFD Simulations of a Hovering Tiltrotor in Ground Effect,” Paper AIAA 2024-1115, AIAA SCITECH 2024 Forum, Orlando, FL, Jan. 8–12, 2024. DOI: 10.2514/6.2024-1115.
10. Wissink, A. M., Jude, D., Jayaraman, B., Roget, B., Lakshminarayanan, V. K., Sitaraman, J., Bauer, A. C., Forsythe, J. R., and Trigg, R. D., “New Capabilities in CREATE-AV Helios Version 11,” Paper AIAA 2021-0235, AIAA Scitech 2021 Forum Proceedings, Virtual Event, Jan. 11–21, 2021. DOI: 10.2514/6.2021-0235.
11. McDaniel, D. R., and Morton, S. A., “Capabilities and Challenges in CFD: A Perspective from the DoD HPCMP CREATE-AV Kestrel Development Team,” Paper AIAA 2017-3789, 55th AIAA Science and Technology Forum and Exposition Proceedings, Grapevine, TX, Jan. 9–13, 2017. DOI: 10.2514/6.2017-3789.
12. Nichols, R. H., and Buning, P. G., “User’s Manual for OVERFLOW 2.3 (Version 2.3d June 2023),” Technical Report, NASA Langley Research Center, <https://overflow.larc.nasa.gov/home/users-manual-for-overflow-2-3>, June 2023.
13. O’Brien, D., “SMEMRD User Manual, V 1.4,” unpublished manual obtained from author, US Army Research, Development, and Engineering Command, 2009.
14. Wissink, A. M., Kamkar, S., Pulliam, T., Sitaraman, J., and Sankaran, V., “Cartesian Adaptive Mesh Refinement for Rotorcraft Wake Resolution,” Paper AIAA 2010-4554, 28th AIAA Applied Aerodynamics Conference Proceedings, Chicago, IL, Jun. 28–Jul. 1 2010. DOI: 10.2514/6.2010-4554.
15. Marcum, D. L., “AFLR3 Unstructured Grid Generator (Version 16.32.50),” Mississippi State University, SimSys Software, October 2024.
16. Sitaraman, J., Lakshminarayanan, V. K., Roget, B., and Wissink, A. M., “Progress in Strand Mesh Generation and Domain Connectivity for Dual-Mesh CFD simulations,” 55th AIAA Aerospace Sciences Meeting, 2017.

17. Biedron, R. T., Carlson, J., Derlaga, J. M., Gnoffo, P. A., Hammond, D. P., Jones, W. T., Kleb, B., Lee-Rausch, E. M., Nielsen, E., Park, M., Rumsey, C., Thomas, J., Thompson, K. B., and Wood, W., “FUN3D Manual: 13.5,” NASA TM 220271, April 2019.